HHS Public Access

Author manuscript

NMR Biomed. Author manuscript; available in PMC 2022 June 30.

Published in final edited form as:

NMR Biomed. 2021 May ; 34(5): e4196. doi:10.1002/nbm.4196.

What is the Optimal Schedule for Multiparametric MRS? A Magnetic Resonance Fingerprinting Perspective

Alexey Kulpanovich[1], **Assaf Tal**[1]

[1]Department of Chemical Physics, Weizmann Institute of Science, 234 Herzel St., Rehovot 7610001, Israel

Summary

Clinical magnetic resonance spectroscopy (MRS) mainly concerns itself with the quantification of metabolite concentrations. Metabolite relaxation values, which reflect the microscopic state of specific cellular and sub-cellular environments, could potentially hold additional valuable information, but are rarely acquired within clinical scan times. By varying the flip angle, repetition time and echo time in a preset way (termed a schedule), and matching the resulting signals to a pre-generated dictionary – an approach dubbed magnetic resonance fingerprinting – it is possible to encode the spins' relaxation times into the acquired signal, simultaneously quantifying multiple tissue parameters for each metabolite. Herein, we optimized the schedule to minimize the averaged root mean square error (RMSE) across all estimated parameters: concentrations, longitudinal and transverse relaxation time, and transmitter inhomogeneity. The optimal schedules were validated in phantoms and, subsequently, in a cohort of healthy volunteers, in a 4.5 mL parietal white matter single voxel and an acquisition time under 5 minutes. The average intra-subject, inter-scan coefficients of variation (CVs) for metabolite concentrations, T_1 and T_2 relaxation times were found to be 3.4%, 4.6% and 4.7% in-vivo, respectively, averaged over all major singlets. Coupled metabolites were quantified using the short echo time schedule entries and spectral fitting, and reliable estimates of glutamate+glutamine, glutathione and myo-inositol were obtained.

Keywords

Magnetic resonance fingerprinting; MRF; magnetic resonance spectroscopy; MRS; Magnetic resonance spectroscopic fingerprinting; MRSF; Multiparametric MRS; T1 relaxation; T2 relaxation

Introduction

Proton Magnetic Resonance Spectroscopy (MRS) quantifies the concentrations of several metabolites, including n-acetyl-asparate (NAA), choline (Cho) and creatine (Cr) containing compounds, myo-inositol (mI) and glutamine and glutamate (Glx); these metabolites act as markers for disease activity in multiple pathologies, ranging from cancer (1–3), Alzheimer's disease (4,5) and dementia (5,6), to traumatic brain injury (7–10) and multiple sclerosis

Corresponding Author/Reprints requests: Assaf Tal, PhD, Department of Chemical Physics, Weizmann Institute of Science, 234 Herzel St., Rehovot 7610001, Israel, Telephone: 972-(0)8-934-4951, FAX: 972-(0)8-934-4123, assaf.tal@weizmann.ac.il.

(11,12). Independent of their concentrations, which reflect the tissue's biochemistry, metabolites' relaxation times (T_1, T_2) provide information about their microscopic environment. For example, the relaxation times of NAA, which is primarily found in neurons (13), reflect the neuronal microenvironment and could act as independent markers of neurodegeneration or inflammation. A large body of evidence for altered metabolite relaxation times exists, in disorders such as multiple sclerosis (14–19), Alzheimer's disease (20–22) and cancer (23–28), to name a few. However, conventional MRS protocols are not set up to measure metabolite T_1 and T_2 values within clinical scan times of approximately 5 minutes or less, and existing sequences for doing so – such as inversion recovery or multi-echo MRS – are not optimized for time efficiency and are rarely implemented in clinical settings.

A second need for multiparametric MRS data arises during signal quantification. The MRS signal is often weighted by various factors: pulsing too rapidly, at time scales of the order of T_1 or shorter, introduces T_1 saturation; non-zero echo times introduce T_2 weighting; and imperfectly calibrated transmitter voltages result in B_{1+} weighting. Correction of this weighting is crucial for accurate quantification of both absolute (in mM) and relative metabolite concentrations, and requires knowing each subject's specific T_1, T_2 and B_{1+} values. Existing approaches often rely on tabulated population averaged values for T_1 and T_2, which could significantly bias the MRS signal (29). In many instances, exact information for a region of interest, pathology, gender, age group and tissue type is simply unavailable. A recent analysis has examined the cumulative effect of both of these benefits for a large number of neuropathologies and regions of interest, based on an extensive body of literature of metabolites' concentration and relaxation values (30): Compared to conventional MRS, multiparametric MRS is predicted to improve the median area underneath the respective receiver operating characteristic curves of each method from 0.72 to 0.86; when confining the analysis to the ten cases showing the largest improvement, the predicted improvement becomes even more marked, increasing from 0.68 for conventional MRS to 0.92 for multiparametric MRS.

Previously, we have demonstrated the benefits of combining a variable schedule with single voxel spectroscopy (29) to simultaneously acquire metabolites' concentrations, T_1 and T_2 relaxation times, alongside the radiofrequency transmitter's inhomogeneity (B_{1+}). This approach, coined Magnetic Resonance Spectroscopic Fingerprinting (MRSF), utilizes a schedule with variable sequence parameters such as the repetition time (TR), echo time (TE) and excitation flip angle (FA), as done in Magnetic Resonance Fingerprinting (31). The schedule encodes the spin parameters (T_1, T_2, B_{1+}) into the time-varying signal, termed a fingerprint. The schedule has a substantial impact on the sequence's ability to encode the spin parameters, and hence, its optimization is a major goal of fingerprinting. There have been several works which have addressed this problem in detail in the context of imaging (32,33). However, the unique sequence topologies of MRS, with their long minimum TRs and TEs, make the aforementioned imaging schedules unsuitable for spectroscopy. Furthermore, the low signal to noise ratio (SNR) associated with MRS plays an important factor in MRSF schedule design; the above works have not considered the effect of schedule length, which directly affects the SNR per schedule entry and, hence, has an important impact on the quality of the spectral MRS data.

In this work, we optimized the MRSF schedule to minimize the average root mean square error (RMSE) of T_1, T_2 and B_{1+}. Several different schedule lengths were considered, while keeping the total acquisition time and SNR per unit time fixed, to determine whether there exists an optimal schedule length. Genetic algorithms with large starting population sizes were used to avoid local minima and accelerate convergence. Several previous works have used surrogate functions to estimate schedule performance, such as the dot product between dictionary elements (32). Here, we used Monte Carlo simulations to explicitly and precisely estimate the RMSE at each optimization step. The quantification of the concentrations and relaxation values using the optimal schedule were assessed in a brain phantom and in a cohort of 14 healthy volunteers.

Methods

MRSF Sequence

Each MRSF schedule consisted of N_{ent} consecutive, distinct entries, each with its own TR, TE and excitation flip angle (FA) in a PRESS sequence. All pulses were designed using an SLR algorithm with a peak radiofrequency amplitude of B_1=18.8 μT ($\gamma B_1 = 800$ Hz); due to the variable flip angle, each excitation pulse had a different bandwidth and, consequently, slice selection gradient. Spins were initially driven into dynamic equilibrium by an initial playout of the schedule without water suppression, which was also used to measure reference water T_1, T_2 and B_{1+} values. The water-derived value of B_{1+} was used to constrain subsequent fittings of metabolite data. Once in dynamic equilibrium, the schedule was repeated N_{avg} times for signal averaging, keeping the total acquisition time $\left(N_{avg}+1\right)\cdot\sum_{i=1}^{N_{ent}} TR_i$ fixed at 5 minutes. We note that, much like for conventional MRS, a variable schedule also enters a dynamic equilibrium very quickly (within a time $\approx 5\cdot T_1$), in which the magnetization vector is identical at the beginning of each repetition of the schedule.

MRSF Schedule Optimization

A range of 9 schedule lengths were optimized (N_{ent}=5, 10, 15, 20, 25, 50, 60, 75 and 100). Optimization minimized the normalized Root Mean Square Error ($\overline{nRMSE}$) of each schedule:

$$\overline{nRMSE} \equiv \frac{1}{M}\sum_{k=1}^{M}\left(nRMSE(T_{1,k}) + nRMSE(T_{2,k})\right). \quad (1)$$

The summation is extended over a fixed set of five equispaced values of $T_{1,k}\in$[750, 1650] ms and $T_{2,k}\in$[125, 350] ms (k=1,…,5), for a total of M=25 terms. To speed up convergence, a fixed value of B_{1+}=1 was assumed. The normalized RMSE for a quantity T is defined as: $nRMSE(T) = \frac{\sqrt{\text{bias}(T)^2 + \text{var}(T)}}{T}$. The normalization by T ensures that relative – and not absolute – deviations are considered; This is similar to minimizing the coefficient of variation (CV), as opposed to the absolute value of the standard deviation. For a given schedule, $\overline{nRMSE}$ (Eq. (1)) was estimated using single-spin Monte-Carlo simulations as

follows: given values of (T_1, T_2, B_{1+}), the corresponding fingerprint was obtained by numerically solving the Bloch equations; noise was added; and fitting to a pre-generated dictionary was carried out. This was repeated 3,000 times, to generate a robust histogram, from which both the bias and variance of T_1 and T_2 could be calculated with a high degree of accuracy. The noise was normally distributed around zero. The noise's standard deviation was calibrated to yield an SNR of 15 for a single, fully relaxed 90̊ excitation, and then scaled as $\sqrt{N_{avg}^{-1}} = \sqrt{\left(\sum_{j=1}^{N_{ent}} TR_j\right)/(5\text{ minutes})}$, to keep the SNR per unit time fixed and ensure a fair comparison between the different schedule lengths.

Optimization was carried out using the built-in genetic algorithm toolbox of MATLAB 2017a (The Mathworks, Natick, MA). To reduce optimization complexity, discrete sets of values for FA=[0°, 5°, …, 150°], TR=[900, 910, …, 1600] ms and TE=[35, 40, …, 150] ms were used. Discretization is supported both by physical intuition, since small changes of a few milliseconds or degrees to sequence parameters are not expected to induce large changes to the acquired fingerprints; and by prior observations that the dictionary space is highly redundant (34–36). To avoid local minima, an initial population size of 500 was used, and the algorithm was repeated four times; all four solutions were evaluated using a higher resolution dictionary (see below), and the optimal solution was retained. The stopping criteria were set to a maximum of 200 generations, and a minimal change of 0.001 in the $\overline{nRMSE}$.

MRSF Schedule Evaluation

Following optimization, $\overline{nRMSE}$ was re-evaluated for each schedule using single-spin Monte-Carlo simulations employing a wider range of equispaced T_1, T_2 and B_{1+} values ($T_1 \in [750, \ldots, 1650]$, $T_2 \in [125, \ldots, 350]$, $B_{1+} \in [0.9, 1.0, 1.1]$ in Eq. (1)). A higher-resolution dictionary was used for fitting ($T_1 \in [600, \ldots, 2500]$ ms, $T_2 \in [50, \ldots, 600]$ ms and $B_{1+} \in [0.8, \ldots, 1.2]$).

To assess the impact of optimization, the performance of each schedule was compared to a randomly generated solution: for a given schedule length (N_{ent}), 20 random schedule were generated and the $\overline{nRMSE}$ was calculated for each. To assess the importance of "spin memory" – that is, the formation of inter-scan coherences between successive entries, which increase the amount of possible T_1 and T_2 weighting – each optimal schedule was randomly reshuffled 20 times; the $\overline{nRMSE}$ was calculated for each reshuffled schedule. Reshuffling was carried out using MATLAB's randperm command, which returns a uniformly randomized reordering of a given vector.

To assess the contribution of each point in the schedule to T_1, T_2 and B_{1+} evaluation, an occlusion test was performed for the N_{ent}=10 case. A point $1 \leq M \leq N_{ent}$ was selected, and the $\overline{nRMSE}$ was evaluated using Monte Carlo simulations as previously described, with the exception that the noise at point M was amplified ten-fold. This was done for all values of $M \in [1, N_{ent}]$.

Phantom Measurements

All measurements were carried out on a Siemens 3T Prisma MRI scanner using the body coil for transmission $\left(B_{1,\,max} = 20\mu T\right)$ and a standard 20-channel receiver head coil (Siemens-Healthineers, Erlangen, Germany). A homogeneous spherical phantom containing 11 mM NAA (T_1/T_2=820/446 ms), 10 mM Cr (T_1/T_2=600/430 ms), 2 mM Cho (T_1/T_2=430/310 ms), 10 mM Glu, 5 mM Lac, 2 mM GABA and 8 mM mI was used. Sodium azide (NaN_3 0.01%) and Gd-DTPA (0.5 mM) were added to prevent microbial growth and reduce T_1 and T_2, respectively. Tabulated values of T_1 and T_2 were recorded using prolonged inversion recovery and spin-echo single-voxel sequences.

A 1.5×1.5×1.5 cm^3 voxel was placed at the phantom's center and shimmed using the built-in shimming routines. The optimal N_{ent}=10 MRSF schedule was used, with a duration of $\sum_{i\,=\,1}^{N_{ent}} TR_i = 14$ seconds per average, N_{avg}=20 averages and a total of 4:54 minutes. The dwell time was 0.5 ms, with 256 ms of acquisition. The acquisition was repeated N_{rep}=22 times, to produce multiple estimates of each peak's parameters and assess the method's bias and standard deviation. The total acquisition time for the entire protocol was 1:45 hours.

Spectra were summed over the averaging dimension, four-fold zero-filled and apodized with a 5 Hz Gaussian kernel along the spectral domain before being Fourier transformed. The peak intensities of NAA (2.01 ppm), Cr (3.0 ppm) and Cho (3.2 ppm) were obtained from the amplitudes of the phased real spectra for each of the N_{ent}=10 schedule entries, producing three separate fingerprints. Fitting to the MRSF dictionary was implemented using MATLAB's fminsearch function, which maximized the dot product of the simulated and measured fingerprint (i.e. minimized its negative). Simulated fingerprints were generated using full 3D Bloch simulations. All three PRESS pulse profiles were taken into account, using a digital phantom with 100×10×10=10000 spins uniformly spread across a $3.5 \times 3.5 \times 3.5\ cm^3$ volume. The number of spins was selected based on convergence of the results to a stable value. To further increase stability and accelerate fitting, the fingerprint of the high-SNR, unsuppressed water reference scan was initially fit to the dictionary to extract the global B_{1+} value, which was then used to constrain fitting of the metabolites' data. Note that the water data is acquired as the system attains dynamic equilibrium.

For each repetition, metabolite concentrations were assessed as follows: all scans with TE=35 ms were summed and fitted using LCModel v6.3c (37). Basis functions were generated for each of the metabolites in the phantom using in-house quantum mechanical simulations written in MATLAB. The first schedule entry of the water signal was used as the reference spectrum. The fitted results from LCModel were scaled to obtain relaxation-corrected, absolute-quantified concentrations as follows: let $\left(s_1, s_2, \ldots, s_{N_{ent}}\right)$ be the simulated fingerprint for the metabolite and $\left(w_1, w_2, \ldots, w_{N_{exc}}\right)$ the simulated fingerprint of the water signal. The metabolite and water signals for each of the schedule entries (after summation of all metabolite averages) are $S_j^{(met)} = \Lambda \cdot C_{met} \cdot s_j \cdot N_{avg}$ and $W_j^{(water)} = \Lambda \cdot C_{water} \cdot w_j$, respectively, where C_{met}, C_{water} are their respective concentrations. The factor Λ accounts for factors which identically affect both acquisitions, such as coil sensitivity and electronics.

The ratio $\sum_{j \in (TE=35\,ms)} S_j^{(met)} / W_1^{(water)}$ equals the output of LCModel when provided with the summed metabolite spectra of the TE=35 ms schedule entries, using the spectrum of the unsuppressed water's first entry as a reference. This ratio also equals $\frac{C_{met} \cdot N_{avg} \cdot \sum_{j \in (TE=35\,ms)} s_j}{c_{water} \cdot w_1}$. Thus, LCModel's output can be converted into absolute concentrations by scaling it by:

$$C_{water} \cdot \frac{1}{N_{avg}} \cdot \frac{w_1}{\sum_j s_j} \tag{2}$$

where the sum in the denominator is over the TE=35 ms schedule entries.

Using the TE=35 ms subset of spectra ensured that no destructive interference between different echo times took place, but also impaired the total SNR of the measurement. To quantitatively assess this loss, the total SNR of four cases was calculated using full 3D Bloch simulations: (i) A conventional PRESS, using the same SLR pulse as the FA=90° MRSF excitation pulse and a TR/TE=1500/35 ms, typical of in-vivo acquisitions which seek to optimize the SNR per unit time (38); (ii) The same as (i), but using TR=5000 ms to minimize T_1 weighting; (iii) Summing all MRSF schedule entries; (iv) Summing just the TE=35 ms subset of MRSF schedule entries. The simulations were carried out for each of the singlets in the phantom (NAA, Cho, Cr) using their measured T_1 and T_2 values, as estimated using MRSF. Results were averaged over all singlets. For each case, three quantities were compared: (i) The normalized voxel volume, equal to the simulated volume of the voxel, divided by its nominal volume. (ii) The weighted voxel volume, given by the normalized voxel volume but also including the effects of T_1 and T_2 relaxations. (iii) The SNR per unit time, normalized to the PRESS TR=5000 ms case. For MRSF, each of these quantities was calculated for each schedule entry, and averaged over all relevant entries (either all entries, or just the TE=35 ms entries).

In-Vivo Experiments

The inter-subject, inter-scan and intra-scan variability of MRSF were assessed in a cohort of 14 healthy volunteers. Participants were scanned after obtaining written informed consent, in accordance with the procedures approved by the Internal Review Board of Emek Medical Center (Afula, Israel). For each volunteer, a T_1-weighted MPRAGE scan (TR/TE/TI=2300/3.03/900 ms, FA=9°, FOV=256×256 mm^2 in plane, 1 mm isotropic resolution) was acquired for voxel placement and tissue segmentation. A single 1.5×1.5×2 cm^3 voxel was positioned in parietal WM region, shimmed using the built-in scanner routines, and scanned using the optimal N_{ent}=10 schedule (TA=4:54 minutes). The MRSF scan was repeated three times, after which the subject was removed and repositioned inside the scanner, and all scans were repeated. In total, each volunteer was scanned a total of 3 × 2 = 6 times.

Metabolite concentrations were estimated using LCModel as described for the phantom. The simulated basis set consisted of Alanine, Aspartate, Creatine, GABA, Glucose, Glutamate, Glutamine, Glutathione, Choline, Lactate, myo-Inositol, NAA, NAAG and Taurine. The MPRAGE images were segmented into white matter (WM), gray matter (GM) and

cerebrospinal fluid (CSF) maps using SPM12 (39), and the fraction of each map in the spectroscopic voxel was calculated (f_{WM}, f_{GM}, f_{CSF}). These were used to normalize metabolite scans by CSF fraction (by dividing by $1 - f_{CSF}$), to calculate the mean water concentration in the voxel ($C_{water} = f_{WM}C_{water}^{WM} + f_{GM}C_{water}^{GM} + f_{CSF}C_{water}^{CSF}$, and to assess reproducibility of voxel positioning.

There is no gold standard in-vivo and hence accuracy could not be assessed. Instead, we've estimated the inter-scan, intra-subject coefficient of variation for each subject ($k = 1, \ldots, 14$) and each measured quantity $Q_{m,n}^{(k)}$ ($Q = T_1, T_2$, concentrations; $m = 1,2$ scan index; $n = 1,2,3$ repetition; $k = 1, \ldots, 14$ subject index): $CV_k = \frac{\sqrt{\left(\frac{1}{3}\sum_{n=1}^{3} \mathrm{var}\left(Q_{1,n}^{(k)}, Q_{2,n}^{(k)}\right)\right)}}{\mathrm{mean}\left(Q_{1,1}^{(k)}, Q_{1,2}^{(k)}, \ldots, Q_{2,3}^{(k)}\right)}$. The average CV per quantity was obtained by: $CV = \sqrt{\sum_{k=1}^{14} CV_k^2}$.

Result

MRSF Schedule Optimization

All optimization algorithm terminated by reaching the minimal tolerance for the target function, indicating a minimum has been reached. Optimization of a single schedule (N_{ent}=50) took about 2.5 hours on Intel i7–4790 desktop computer running in parallel on 4 cores. Total run time was 90 hours. Fig. 1a shows the N_{ent}=10 optimal schedule, and Supplementary Table S1 lists the full schedules for each N_{ent}. Supplementary Fig. S1 shows the time dynamics of M_z of a single spin with T_1=1000 ms, T_2=200 ms as it enters dynamic equilibrium following several iterations of the N_{ent}=10 schedule.

The optimal $\overline{nRMSE}$ varied between 3%−4%, indicating little to no dependence on N_{ent}. Fig. 1b shows the mean $\overline{nRMSE}$ for the optimal schedules (averaged over all four starting conditions) as a function of N_{ent}. The N_{ent}=10 schedule was chosen for phantom and in-vivo validations. Shuffling the order of schedule entries (Fig. 1b) approximately doubled the $\overline{nRMSE}$, indicating spin-memory plays an important role in schedule performance. Using completely random schedules triples and even quadruples the optimal $\overline{nRMSE}$, indicating schedule optimization is important for high quality estimates of relaxation parameters. The dependence of $\overline{nRMSE}$ on the SNR for all schedules is shown in Fig. 1c, where it approximately scales as SNR^{-1}, which is typical for many quantification algorithms (40). Fig. 1d shows the results of the occlusion test, which demonstrate T_1, T_2 and B_{1+} information is not encoded equally along the schedule. For example, T_2 estimation is most sensitive to perturbations in schedule entries 1, 2, 3, 7 and 10, while T_1 estimation is sensitive to entries 5, 6 and 8. This information is useful when examining the dictionary fitting residuals; for example, larger residuals for entries 5, 6 or 8 would indicate T_1 estimation could be compromised without impairing T_2 estimation.

Phantom Measurements

Table 1 lists estimated concentrations and relaxation times for the major singlets (NAA at 2.01 ppm, Cr at 3 ppm and Cho at 3.2 ppm) in the phantom. The CVs for T_1 quantification

were 4%, 6.7% and 10.3%, respectively; the differences arise from the fact that NAA, Cr and Cho differ in their SNRs, which were 14.7, 14 and 9.7. The SNR was quantified from the first average of the first schedule entry using peak heights divided by the standard deviation of the noise, and was subsequently relaxation-corrected and scaled to correspond to a 90° homogeneous (B_{1+}=1.0) excitation pulse; the scaling coefficient was obtained via full 3D Bloch simulations using each peak's measured T_1, T_2 and B_{1+}. The CVs for T_2 were 6.4%, 5.9% and 14.8%. B_{1+} was quantified using the water resonance, with a CV of less than 1%. The concentrations of each singlet were quantified from the results of the LCModel fits (to the summed TE=35 ms entries) and the relaxation correction factors (Eq. (2)), and yielded deviations of 0.1 mM or less from their true values, with CVs between 3.5%-5%. Overall, the phantom results exhibit minimal bias, with CVs that increase as SNR decreases (similarly to Fig. 1c). While LCModel produced reliable fits (CRLB<10%) for all metabolites in the phantom, they are omitted from the Table; the current MRSF framework uses the uncoupled Bloch equations which do not properly model the behavior of coupled resonances. Without true, reliable estimates of their T_1 and T_2 values, the concentrations of the coupled metabolites could not be accurately quantified.

Fig. 2 showcases representative phantom results. Voxel positioning is shown in Fig. 2a. Spectra from the individual MRSF schedule entries are shown in Fig. 2b after averaging. The mean individual fingerprints of NAA, Cr and Cho are shown in Fig. 2c. The overall shapes of the fingerprints are very similar, but the differences between them are sufficiently large compared to their variability. Also note the fingerprints shown are divided by their L_2-norms; their un-normalized relative magnitudes can differ significantly due to concentration, T_1 and T_2 differences. Fig. 2d shows the mean±standard deviation of the dictionary fitting residual, i.e. the difference between the experimentally measured and simulated fingerprints, over all N_{rep}=22 repetitions. The means are within a standard deviation (shaded region) zero, indicating the high quality of the model used. This is a necessary – albeit not sufficient – condition for an accurate and precise estimation of T_1, T_2 and B_{1+}. Taken together with the results of the occlusion test (Fig. 1d), this plot can be used to diagnose potential problems with the fitting procedure: large deviations at particular entries could affect the estimation of certain parameters more than others. In the current dataset, no such deviations are observed. Figs. 2e, 2f and 2g show boxplots of the differences between the tabulated phantom T_1, T_2 and concentrations, and those estimated from each of the 22 repetitions. The centers (medians) of the boxplots indicate the method's accuracy (bias), while their width (inter-quartile range) indicates the method's precision.

In-Vivo Experiments

Fig. 3a shows voxel placement for a representative volunteer. Average tissue fractions were $f_{WM} = 88.8\% \pm 4.5\%$, $f_{GM} = 10.8\% \pm 4.2\%$ and $f_{CSF} = 0.4\% \pm 0.3\%$, indicating reproducible voxel positioning and mostly WM content. The average SNR of the major singlets (NAA, Cr and Cho), calculated as for the phantom, was 11.3, 5.7 and 5.1, respectively. The linewidth of NAA was stable throughout: the mean full width at half maximum (FWHM) taken over all subjects was 7.7 Hz, and the mean deviation over the scan – quantified by dividing the standard deviation of the FWHM by its mean over 20 averages, and averaging the results over all scans and all subjects – was 11.2% (i.e. < 1 Hz). Such changes are consistent with

normal physiological noise and indicate overall good measurement stability. The effect of any linewidth alterations during the measurement are already encapsulated in the reported CVs.

Table 3 summarizes the results for all reliably quantified metabolites (CRLB≤20%), obtained by fitting the summed TE=35 ms spectrum of each volunteer using LCModel. It is impossible to assess accuracy (bias) in-vivo, since the true concentrations and relaxation values are unknown; thus, the Table lists the inter-subject mean±standard deviation, and also notes the inter-scan, intra-subject CV in parentheses; it is this quantity which describes MRSF's precision. For the major singlets (NAA, Cr, Cho), T_1 and T_2 were quantified using the MRSF pipeline. For coupled metabolites, the relaxation values appearing in the Table are taken from the literature (41–46); we could not find references quantifying GSH's transverse relaxation times at 3T, and a T_2=100 ms was assumed. These relaxation values were used to compute the relaxation-correction factor (Eq. (2)) necessary for absolute quantification. No attempts were made to remove any outliers while compiling Table 3. Note the in-vivo CVs on T_1 and T_2 (Table 3) are better in most cases than those recorded in the phantom (Table 1). This is because the relaxation times encountered in the phantom are quite different from those in-vivo (e.g. T_2s on the order of 400 ms), while our schedules were optimized for in-vivo values of T_1 and T_2.

Fig. 3b shows spectra from all N_{ent}=10 schedule entries from a representative volunteer. Fig. 3c shows the mean±standard deviation of the fingerprints of NAA, Cr and Cho, taken over all 14 volunteers, while Fig. 3d shows the residuals (compare to the phantom results in Figs. 2c and 2d). Figs. 3e, 3f and 3g present the distribution of measured T_1, T_2 values and concentrations for NAA, Cr and Cho from all volunteers, scans and repetitions. Finally, Fig. 3h presents a spectrum from a sample volunteer, obtained by summing just the TE=35 ms schedule entries, and its corresponding quality of the LCModel fit.

Discussion

In a previous publication we've outlined the general methodology of a variable-schedule multiparametric MRS framework (29). The current work extends the framework by optimizing the schedule and schedule length; by showing that LCModel fitting can also be used to fit the short echo time (TE=35 ms) schedule entries to obtain metabolite concentrations even for J-coupled metabolites, at an SNR that is comparable to a long-TR PRESS (Table 2); by shortening the total scan time to under 5 minutes; and by using a larger cohort of 14 volunteers to demonstrate the robustness of the proposed pipeline. Our in-vivo data, collected from a 4.5 mL voxel using standard hardware, shows this approach produces average inter-scan CVs of 3.4%, 4.6% and 4.7% for metabolite concentrations, T_1 and T_2 relaxation times, respectively, averaged over all major singlets.

Schedule optimization plays an important role in multiparametric MRS, as shown by Fig. 1b. Our results show that the $\overline{nRMSE}$ can be brought down to around 3–4% for an SNR of 15 for the different schedule lengths considered ($5 \leq N_{ent} \leq 100$). Schedules with as few as N_{ent}=5 entries also exhibit fairly low $\overline{nRMSE}$s. This is particularly attractive for incorporating fingerprinting schedules with other time-consuming acquisitions; for example,

using echo planar spectroscopic imaging, a single 2D-MRSI slice can be sampled in under a minute. This leaves ample time to swap the conventional averaging dimension with a fingerprinting schedule to produce spatial multiparametric metabolite maps of the major singlets.

While we acquired our data using a PRESS with a variable excitation flip angle, the optimized schedules in Supplementary Table S1 were based on a single-spin pulse-acquire topology and could be applied to other popular single-voxel spin-echo based MRS localization modules, such as semiLASER (47). Not all modules are a-priori compatible, though: LASER (48) uses an adiabatic excitation; SPECIAL (49) uses a preparatory inversion pulse; and STEAM (50) and STRESS (51,52) both acquire stimulated echoes. These sequences' spin evolution is somewhat different from a simple pulse-acquire sequence, and, while the schedules in Table S1 would likely perform well for them, they would likely require re-optimization for best results.

The Optimal Schedules do not Substantially Impair SNR

The variable schedule implies that MRSF acquisitions are sub-optimal from an SNR per unit time perspective. In this particular work, we only used the short echo time (TE=35 ms) spectra for quantifying metabolites' concentrations. As shown by Table 2, when compared to an equivalent PRESS sequence with an optimal $TR=1.2\cdot T_1$ and an FA=90° excitation pulse, the total SNR of the MRSF dataset is only 60% (when using the subset of TE=35 ms schedule entries) of that of the optimal PRESS sequence, averaged over all singlets using in-vivo values for T_1 and T_2 and assuming $B_{1+}=1.0$. This reduction in SNR, however, is less severe than for an equivalent and optimal STEAM sequence. The reduction is even less severe – only 20% - when compared to long TR acquisitions, which are often favored as a method for minimizing T_1 weighting. Table 2 also reveals that a further increase in total SNR is possible by incorporating the long echo time schedule entries. Since such an approach would mix different echo times, a simple summation would confound quantification; a more correct approach would require a more advanced spectral fitting algorithms. Suitable approaches have been used in fitting 2D and multi-TE datasets, and could likely be extended to handle the full MRSF dataset (53).

Coupled Metabolites' Concentrations Can Be Estimated Using Short Echo Times

The use of short echo time scans produces usable estimates of coupled metabolites, including myo-Inositol and Glx, even if their relaxation times are not quantified. This is reflected in the CRLBs estimated by LCModel (Table 3), which are in-line with other single-voxel MRS acquisitions in WM (42,45,46,54–56).

Dictionary Fitting for Coupled Metabolites Remains Challenging

The quantum nature of J-coupled metabolites excludes them from being fit to the simple Bloch-equation framework proposed in the current work. Further research into appropriate models which combine quantum mechanical evolution in Liouville space with relaxation is still required before dictionary-fitting approaches can be successfully applied to such coupled metabolites. Thus, the current work did not estimate the relaxation values of coupled metabolites. We note that, unlike NAA, Cr and Cho, where the per-subject values of

T_1 and T_2 were used for relaxation correction in Table 3 (using Eq. (2)), the estimation of coupled metabolites' concentrations was done using literature values for T_1 and T_2.

A related challenge concerns the use of spectral fitting to generate reproducible fingerprints. We have attempted to spectrally fit each of the individual N_{ent}=10 entries using LCModel, construct fingerprints for each metabolites – coupled and uncoupled alike – and fit those to the dictionary of 3D Bloch-simulated fingerprints using our described pipeline. Results have yielded either particularly large coefficients of variation or unrealistic estimates of T_1 and T_2, and, currently, the use of spectral fitting for generating individual fingerprints remains challenging. This holds true even for the singlets of NAA, Cr and Cho, for which spectral fitting produced up to two-fold larger coefficients of variation and biases.

Most metabolites have more than one spectral peak associated with them, often with differing relaxation values – e.g., Cr's two singlets at 3.03 and 3.92 ppm (46). Hence, each peak or subgroup will have a different fingerprint associated with it. Using peak amplitudes (or integrated areas) to generate fingerprints, as done herein, effectively decouples the different peaks and avoids introducing any correlations between their estimated fingerprints. It remains to be seen whether spectral fitting will be able to generate reliable fingerprints in the future; if so, separate basis functions will have to be used for each chemical sub-group, to ensure their fingerprints remain unbiased.

Extending MRSF to Include Additional Spin Parameters

The schedule optimization only modeled T_1 and T_2 relaxation and transmitter inhomogeneity. The basic PRESS sequence has limited sensitivity to other metabolite parameters, such as diffusion or chemical exchange. Incorporating those would require investigating different sequence topologies; for example, adding diffusion weighting gradients in between the volume selective pulses of the PRESS sequence, as done for diffusion weighted MRS (57,58). One should however undertake such endeavors cautiously: the addition of model parameters often increases the estimation errors on those parameters. Additional parameters also increase the computational complexity of the simulations required for dictionary generation. Even though we decompose the 3D spin simulations into successive 1D simulations (59), simulating a single fingerprint requires on the order of ~ 1 second. This prohibits MRSF from generating a-priori even the simplest dictionaries, instead forcing dictionary matching to use real-time search algorithms, leading to a post-processing duration of approximately one minute to extract the relaxation parameters of all three singlets. This could be mitigated via the use of neural networks, which can search even high dimensional dictionary spaces within milliseconds (60).

Additional Caveats

The current study focused on a single region of interest and a particular voxel size. It should be noted that the CVs derived herein will depend on the quality and SNR of the spectral data. For example, the SNR of deep gray matter voxels might be lower due to reduced coil sensitivity and, consequently, their CVs will likely be higher. Similarly, smaller voxels, placed in smaller anatomical structures, might yield lower SNR and higher CVs. Thus, a careful re-evaluation of the method's reproducibility must be carried out on a per-study

basis, and until such additional experimental data is made available, any claims about wider applicability in the brain remain conjecture.

Conclusion

By optimizing the schedule, MRSF can be used to acquire the relaxation values of the major singlets, without significantly impairing the quantification of metabolite concentrations of both coupled and uncoupled resonances. Monitoring the unsuppressed water signal as the system is driven into dynamic equilibrium produces estimates of water's T_1 and T_2 constants as well. The ability to acquire per-subject multiparametric spectroscopic data provides more accurate and robust absolute quantification of metabolite concentrations. Furthermore, ample evidence exists that metabolite relaxation times change in multiple neuropathologies, making them potential biomarkers. The multiparametric framework proposed herein thus also enhances the clinical relevance of single voxel MRS, all within a clinical timeframe of under five minutes.

Supplementary Material

Refer to Web version on PubMed Central for supplementary material.

Sponsors, Grants & Funding:

Assaf Tal acknowledges the support of the Minerva Foundation, Monroy-Marks Career Development Fund, and the historic generosity of the Harold Perlman Family. This work was supported by NIH grant R21 NS112853-01.

List of Abbreviations

CRLB	Cramer Rao lower bound
CSF	Cerebrospinal fluid
CV	Coefficient of Variation
FA	Excitation flip angle
FWHM	Full width at half maximum
GM	Gray matter
MRF	Magnetic Resonance Fingerprinting
MRS	Magnetic Resonance Spectroscopy
MRSF	Magnetic Resonance Spectroscopic Fingerprinting
NAA	n-acetyl-aspartate
PRESS	Point resolved spectroscopy
RMSE	Root mean square error
SNR	Signal to noise ratio

SPM	Statistical Parametric Mapping
tCho	Total choline
tCr	Total creatine
TE	Echo time
TR	Repetition time
WM	White matter

References

1. Gillies RJ, Morse DL. In vivo magnetic resonance spectroscopy in cancer. Annu Rev Biomed Eng 2005;7:287–326. [PubMed: 16004573]
2. Garcia-Figueiras R, Baleato-Gonzalez S, Padhani AR, Oleaga L, Vilanova JC, Luna A, Cobas Gomez JC. Proton magnetic resonance spectroscopy in oncology: the fingerprints of cancer? Diagn Interv Radiol 2016;22(1):75–89. [PubMed: 26712681]
3. Bolan PJ, Nelson MT, Yee D, Garwood M. Imaging in breast cancer: magnetic resonance spectroscopy. Breast Cancer Research 2005;7(4):149. [PubMed: 15987466]
4. Soher BJ, Doraiswamy PM, Charles HC. A review of 1H MR spectroscopy findings in Alzheimer's disease. Neuroimaging clinics of North America 2005;15(4):847–852, xi. [PubMed: 16443495]
5. Huang W, Alexander GE, Chang L, Shetty HU, Krasuski JS, Rapoport SI, Schapiro MB. Brain metabolite concentration and dementia severity in Alzheimer's disease: a (1)H MRS study. Neurology 2001;57(4):626–632. [PubMed: 11524470]
6. Magierski R, Sobow T. Magnetic resonance spectroscopy in the diagnosis of dementia with Lewy bodies. Biomed Res Int 2014;2014:809503. [PubMed: 25110697]
7. Hetherington HP, Hamid H, Kulas J, Ling G, Bandak F, de Lanerolle NC, Pan JW. MRSI of the medial temporal lobe at 7 T in explosive blast mild traumatic brain injury. Magnetic resonance in medicine 2014;71(4):1358–1367. [PubMed: 23918077]
8. Gasparovic C, Yeo R, Mannell M, Ling J, Elgie R, Phillips J, Doezema D, Mayer AR. Neurometabolite concentrations in gray and white matter in mild traumatic brain injury: an 1H-magnetic resonance spectroscopy study. J Neurotrauma 2009;26(10):1635–1643. [PubMed: 19355814]
9. Kirov II, Tal A, Babb JS, Lui YW, Grossman RI, Gonen O. Diffuse axonal injury in mild traumatic brain injury: a 3D multivoxel proton MR spectroscopy study. J Neurol 2013;260(1):242–252. [PubMed: 22886061]
10. Kirov II, Tal A, Babb JS, Reaume J, Bushnik T, Ashman TA, Flanagan S, Grossman RI, Gonen O. Proton MR spectroscopy correlates diffuse axonal abnormalities with post-concussive symptoms in mild traumatic brain injury. J Neurotrauma 2013;30(13):1200–1204. [PubMed: 23339670]
11. Narayana PA. Magnetic resonance spectroscopy in the monitoring of multiple sclerosis. Journal of Neuroimaging 2005;15:46S–57S. [PubMed: 16385018]
12. Kirov II, Tal A, Babb JS, Herbert J, Gonen O. Serial proton MR spectroscopy of gray and white matter in relapsing-remitting MS. Neurology 2013;80(1):39–46. [PubMed: 23175732]
13. Moffett JR, Ross B, Arun P, Madhavarao CN, Namboodiri AM. N-Acetylaspartate in the CNS: from neurodiagnostics to neurobiology. Prog Neurobiol 2007;81(2):89–131. [PubMed: 17275978]
14. van Walderveen MA, Barkhof F, Pouwels PJ, van Schijndel RA, Polman CH, Castelijns JA. Neuronal damage in T1-hypointense multiple sclerosis lesions demonstrated in vivo using proton magnetic resonance spectroscopy. Ann Neurol 1999;46(1):79–87. [PubMed: 10401783]
15. Srinivasan R, Sailasuta N, Hurd R, Nelson S, Pelletier D. Evidence of elevated glutamate in multiple sclerosis using magnetic resonance spectroscopy at 3 T. Brain 2005;128(Pt 5):1016–1025. [PubMed: 15758036]

16. Kirov II, Liu S, Fleysher R, Fleysher L, Babb JS, Herbert J, Gonen O. Brain metabolite proton T2 mapping at 3.0 T in relapsing-remitting multiple sclerosis. Radiology 2010;254(3):858–866. [PubMed: 20177098]
17. Kirov II, Fleysher L, Fleysher R, Patil V, Liu S, Gonen O. Age dependence of regional proton metabolites T2 relaxation times in the human brain at 3 T. Magn Reson Med 2008;60(4):790–795. [PubMed: 18816831]
18. Schubert F, Seifert F, Elster C, Link A, Walzel M, Mientus S, Haas J, Rinneberg H. Serial 1H-MRS in relapsing-remitting multiple sclerosis: effects of interferon-beta therapy on absolute metabolite concentrations. MAGMA 2002;14(3):213–222. [PubMed: 12098564]
19. Brief EE, Vavasour IM, Laule C, Li DK, Mackay AL. Proton MRS of large multiple sclerosis lesions reveals subtle changes in metabolite T(1) and area. NMR Biomed 2010;23(9):1033–1037. [PubMed: 20963799]
20. Moats RA, Ernst T, Shonk TK, Ross BD. Abnormal cerebral metabolite concentrations in patients with probable Alzheimer disease. MagnResonMed 1994;32:110–115.
21. Dumoulin MC, Zimmerman EA, Hurd R, Hancu I. Increased brain metabolite T2 relaxation times in patients with Alzheimer's disease. 2005; Miami.
22. Christiansen P, Schlosser A, Henriksen O. Reduced N-acetylaspartate content in the frontal part of the brain in patients with probable Alzheimer's disease. Magn Reson Imaging 1995;13(3):457–462. [PubMed: 7791555]
23. Sijens PE, Oudkerk M. 1H chemical shift imaging characterization of human brain tumor and edema. Eur Radiol 2002;12(8):2056–2061. [PubMed: 12136324]
24. Manton DJ, Lowry M, Blackband SJ, Horsman A. Determination of proton metabolite concentrations and relaxation parameters in normal human brain and intracranial tumours. NMR Biomed 1995;8(3):104–112. [PubMed: 8579997]
25. Isobe T, Matsumura A, Anno I, Yoshizawa T, Nagatomo Y, Itai Y, Nose T. Quantification of cerebral metabolites in glioma patients with proton MR spectroscopy using T2 relaxation time correction. Magn Reson Imaging 2002;20(4):343–349. [PubMed: 12165353]
26. Usenius JP, Kauppinen RA, Vainio PA, Hernesniemi JA, Vapalahti MP, Paljarvi LA, Soimakallio S. Quantitative metabolite patterns of human brain tumors: detection by 1H NMR spectroscopy in vivo and in vitro. J Comput Assist Tomogr 1994;18(5):705–713. [PubMed: 8089316]
27. Li Y, Srinivasan R, Ratiney H, Lu Y, Chang SM, Nelson SJ. Comparison of T(1) and T(2) metabolite relaxation times in glioma and normal brain at 3T. J Magn Reson Imaging 2008;28(2):342–350. [PubMed: 18666155]
28. Landheer K, Sahgal A, Myrehaug S, Chen AP, Cunningham CH, Graham SJ. A rapid inversion technique for the measurement of longitudinal relaxation times of brain metabolites: application to lactate in high-grade gliomas at 3 T. NMR Biomed 2016;29(10):1381–1390. [PubMed: 27455374]
29. Kulpanovich A, Tal A. The application of magnetic resonance fingerprinting to single voxel proton spectroscopy. NMR in biomedicine 2018;31(11):e4001. [PubMed: 30176091]
30. Kirov II, Tal A Potential clinical impact of multiparametric quantitative MR spectroscopy in neurological disorders: A review and analysis. Magnetic resonance in medicine 2019.
31. Ma D, Gulani V, Seiberlich N, Liu K, Sunshine JL, Duerk JL, Griswold MA. Magnetic resonance fingerprinting. Nature 2013;495(7440):187–192. [PubMed: 23486058]
32. Cohen O, Rosen MS. Algorithm comparison for schedule optimization in MR fingerprinting. Magn Reson Imaging 2017;41:15–21. [PubMed: 28238942]
33. Zhao B, Haldar JP, Setsompop K, Wald LL. Optimal experiment design for magnetic resonance fingerprinting. 2016. IEEE. p 453–456.
34. Wang Z, Zhang J, Cui D, Xie J, Lyu M, Hui E, Wu E. Magnetic Resonance Fingerprinting using A Fast Dictionary Searching Algorithm: MRF-ZOOM. IEEE Trans Biomed Eng 2018.
35. Mazor G, Weizman L, Tal A, Eldar YC. Low-rank magnetic resonance fingerprinting. Medical physics 2018;45(9):4066–4084.
36. Bo Z, Bilgic B, Adalsteinsson E, Griswold MA, Wald LL, Setsompop K. Simultaneous multislice magnetic resonance fingerprinting with low-rank and subspace modeling. Conf Proc IEEE Eng Med Biol Soc 2017;2017:3264–3268.

37. Provencher SW. Automatic quantitation of localized in vivo 1H spectra with LCModel. NMR in biomedicine 2001;14(4):260–264. [PubMed: 11410943]
38. Goelman G, Liu S, Hess D, Gonen O. Optimizing the efficiency of high-field multivoxel spectroscopic imaging by multiplexing in space and time. Magnetic resonance in medicine 2006;56(1):34–40. [PubMed: 16767711]
39. Penny WD, Friston KJ, Kiebel SJ, Nichols TE. Statistical Parametric Mapping: The Analysis of Functional Brain Images: Academic Press; 2006. 656 p.
40. Bartha R Effect of signal-to-noise ratio and spectral linewidth on metabolite quantification at 4 T. NMR in biomedicine 2007;20(5):512–521. [PubMed: 17205487]
41. Ganji SK, Banerjee A, Patel AM, Zhao YD, Dimitrov IE, Browning JD, Brown ES, Maher EA, Choi C. T2 measurement of J-coupled metabolites in the human brain at 3T. NMR in biomedicine 2012;25(4):523–529. [PubMed: 21845738]
42. Traber F, Block W, Lamerichs R, Gieseke J, Schild HH. 1H metabolite relaxation times at 3.0 tesla: Measurements of T1 and T2 values in normal brain and determination of regional differences in transverse relaxation. J Magn Reson Imaging 2004;19(5):537–545. [PubMed: 15112302]
43. Wansapura JP, Holland SK, Dunn RS, Ball WS Jr., NMR relaxation times in the human brain at 3.0 tesla. J Magn Reson Imaging 1999;9(4):531–538. [PubMed: 10232510]
44. Choi IY, Lee P. Doubly selective multiple quantum chemical shift imaging and T(1) relaxation time measurement of glutathione (GSH) in the human brain in vivo. NMR in biomedicine 2013;26(1):28–34. [PubMed: 22730142]
45. Ethofer T, Mader I, Seeger U, Helms G, Erb M, Grodd W, Ludolph A, Klose U. Comparison of longitudinal metabolite relaxation times in different regions of the human brain at 1.5 and 3 Tesla. Magnetic resonance in medicine 2003;50(6):1296–1301. [PubMed: 14648578]
46. Mlynarik V, Gruber S, Moser E. Proton T (1) and T (2) relaxation times of human brain metabolites at 3 Tesla. NMR in biomedicine 2001;14(5):325–331. [PubMed: 11477653]
47. Scheenen TW, Klomp DW, Wijnen JP, Heerschap A. Short echo time 1H-MRSI of the human brain at 3T with minimal chemical shift displacement errors using adiabatic refocusing pulses. Magnetic resonance in medicine 2008;59(1):1–6. [PubMed: 17969076]
48. Garwood M, DelaBarre L. The return of the frequency sweep: designing adiabatic pulses for contemporary NMR. J Magn Reson 2001;153(2):155–177. [PubMed: 11740891]
49. Mekle R, Mlynarik V, Gambarota G, Hergt M, Krueger G, Gruetter R. MR spectroscopy of the human brain with enhanced signal intensity at ultrashort echo times on a clinical platform at 3T and 7T. Magnetic resonance in medicine 2009;61(6):1279–1285. [PubMed: 19319893]
50. Frahm J, Bruhn H, Gyngell ML, Merboldt KD, Hanicke W, Sauter R. Localized proton NMR spectroscopy in different regions of the human brain in vivo. Relaxation times and concentrations of cerebral metabolites. Magnetic resonance in medicine 1989;11(1):47–63. [PubMed: 2747516]
51. Volovyk O, Tal A. Application of phase rotation to STRESS localization scheme at 3 T. Magnetic resonance in medicine 2018;79(5):2481–2490. [PubMed: 28972290]
52. Tal A, Gonen O. Spectroscopic localization by simultaneous acquisition of the double-spin and stimulated echoes. Magnetic resonance in medicine 2015;73(1):31–43. [PubMed: 24664399]
53. Chong DG, Kreis R, Bolliger CS, Boesch C, Slotboom J. Two-dimensional linear-combination model fitting of magnetic resonance spectra to define the macromolecule baseline using FiTAID, a Fitting Tool for Arrays of Interrelated Datasets. MAGMA 2011;24(3):147–164. [PubMed: 21424575]
54. Wang Y, Li SJ. Differentiation of metabolic concentrations between gray matter and white matter of human brain by in vivo H-1 magnetic resonance spectroscopy. Magnetic resonance in medicine 1998;39(1):28–33. [PubMed: 9438434]
55. Pouwels PJ, Frahm J. Regional metabolite concentrations in human brain as determined by quantitative localized proton MRS. Magnetic resonance in medicine 1998;39(1):53–60. [PubMed: 9438437]
56. Maghsudi H, Schmitz B, Maudsley AA, Sheriff S, Bronzlik P, Schutze M, Lanfermann H, Ding X. Regional Metabolite Concentrations in Aging Human Brain: Comparison of Short-TE Whole Brain MR Spectroscopic Imaging and Single Voxel Spectroscopy at 3T. Clin Neuroradiol 2019.

57. Wood ET, Ercan AE, Branzoli F, Webb A, Sati P, Reich DS, Ronen I. Reproducibility and optimization of in vivo human diffusion-weighted MRS of the corpus callosum at 3T and 7T. NMR in biomedicine 2015;28(8):976–987. [PubMed: 26084563]

58. Kan HE, Techawiboonwong A, van Osch MJ, Versluis MJ, Deelchand DK, Henry PG, Marjanska M, van Buchem MA, Webb AG, Ronen I. Differences in apparent diffusion coefficients of brain metabolites between grey and white matter in the human brain measured at 7 T. Magnetic resonance in medicine 2012;67(5):1203–1209. [PubMed: 22083562]

59. Zhang Y, An L, Shen J. Fast computation of full density matrix of multispin systems for spatially localized in vivo magnetic resonance spectroscopy. Medical physics 2017;44(8):4169–4178. [PubMed: 28548302]

60. Cohen O, Zhu B, Rosen MS. MR fingerprinting Deep RecOnstruction NEtwork (DRONE). Magnetic resonance in medicine 2018;80(3):885–894. [PubMed: 29624736]

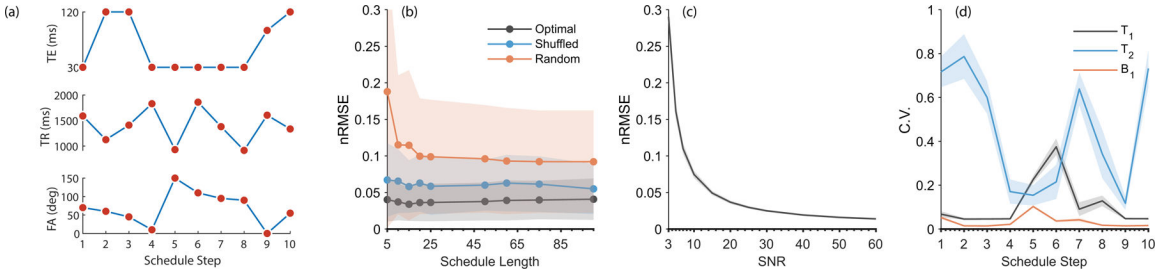

Figure 1.

Simulation results. (a.) The optimal schedule for N_{ent}=10, used for the phantom and in-vivo measurements. (b.) $\overline{nRMSE}$ as a function of schedule length (N_{ent}). Black: optimized schedule. The line corresponds to the mean, while the shaded regions correspond to one standard deviation, taken over four optimization results. Blue: $\overline{nRMSE}$ after reshuffling the order of the schedule entries. This indicates the order of excitations is meaningful, and supports the existence of "spin memory" between consecutive entries. Mean and standard deviation are taken over 20 random reshuffles. Red: $\overline{nRMSE}$ for 20 randomly generated schedules. Overall, optimization yields a three-fold improvement over a randomly generated schedule. (c.) $\overline{nRMSE}$ as a function of SNR, showing an approximate inverse relationship typical of many quantification algorithms. The black line corresponds to the mean over all optimized schedule lengths (N_{ent}), while the very narrow shaded patch corresponds to the standard deviation. (d.) Results of the occlusion test, showing how different points along the N_{ent}=10 schedule affect the estimation of various parameters (T_1, T_2 and B_{1+}). For example, points 5 and 6 along the schedule are particularly important for T_1 quantification.

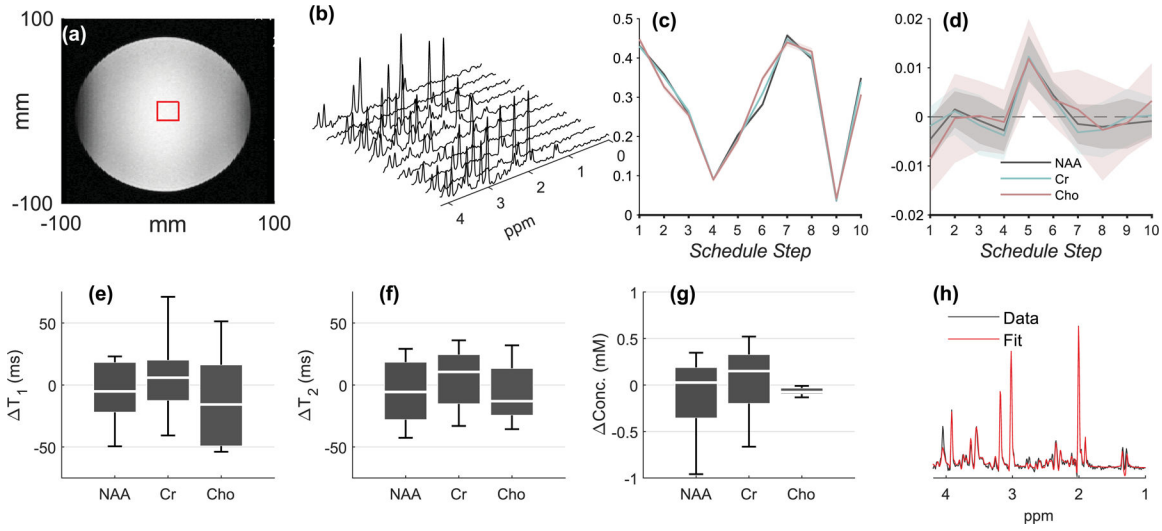

Figure 2.

Phantom results. (a.) Voxel placement. (b.) Spectra from all N_{ent}=10 schedule entries from a single MRSF acquisition, after summation of N_{avg}=20 averages. (c.) The normalized fingerprints of NAA, Cr and Cho from all N_{rep}=22 repetitions (mean±standard deviation). The similarity between different scans is so high that the outlines of the standard deviation can barely be seen. (d.) The mean±standard deviation of the residual for NAA, Cr, Cho, taken over N_{rep}=22 repetitions. All non-zero residuals are either within 1–2 standard deviations from zero, indicating the overall robustness of the dictionary fitting process. (e.) Box plots (median, inter-quartile range and whiskers) for ΔT_1, the difference between the estimated and "true" T_1 in the phantom (as measured using a long inversion recovery experiment), from all N_{rep}=22 repetitions. The schedule's precision (standard deviation) is reflected by the width of the boxplot, while its accuracy (bias) is reflected by its distance from the $\Delta T_1 = 0$ line. (f,g.) Boxplots for ΔT_2 (as measured by a long multi-echo single voxel experiment) and Δconcentrations. (h.) Summed TE=35 ms schedule entries and corresponding LCModel fit from one of the 5-minute N_{rep}=22 repetitions. This fit was used to assess concentrations, as explained in the Methods section.

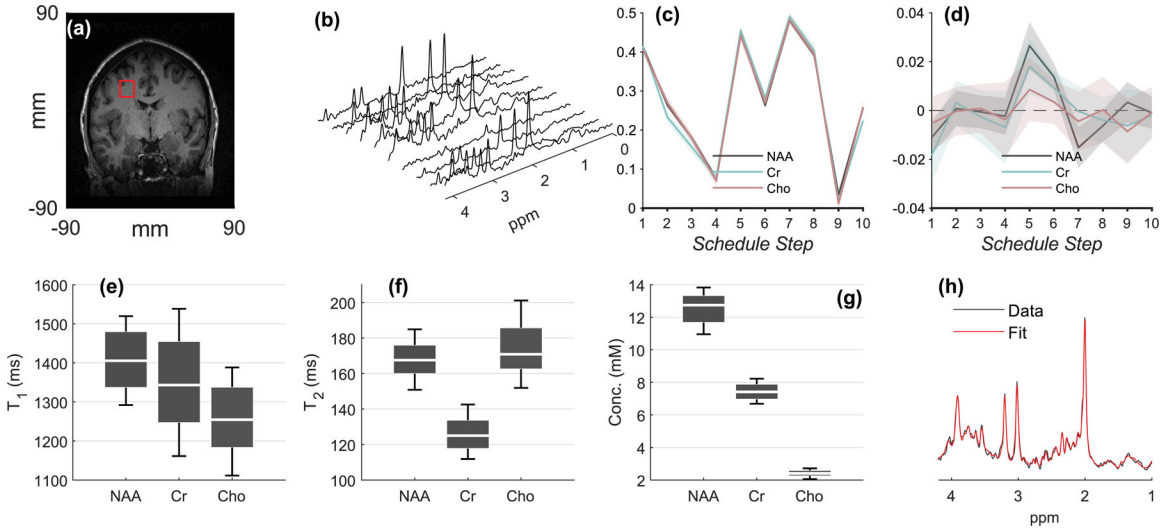

Figure 3.

In-vivo results. The plot follows a similar layout to Fig. 2. (a.) Voxel placement from a representative volunteer. (b.) Spectra from all N_{ent}=10 schedule entries from the same volunteer, after summation of N_{avg}=20 averages. (c.) The normalized fingerprints of NAA, Cr and Cho from the same volunteer (mean±standard deviation for all 3×2=6 scans). (d.) mean±standard deviation of the residual for NAA, Cr, Cho, taken over N_{rep}=22 repetitions. All non-zero residuals are either within 1–2 standard deviations from zero, indicating the overall robustness of the dictionary fitting process. (e-g.) Box plots for the CVs of T_1, T_2 and concentrations from all N_{subj}=14 volunteers. (h.) Summed TE=35 ms schedule entries and corresponding LCModel fit from a representative 5-minute scan from a single volunteer. This fit was used to assess concentrations, as explained in the Methods section.

Table 1.

Phantom quantification results. Results for concentrations, T_1 and T_2 are shown as deviations from their gold standard values. Mean±standard deviations are taken over all N_{rep}=22 repetitions. Concentrations were quantified using the summed TE=35 ms acquisitions, as fit by LCModel. CRLBs output by LCModel are averaged over all repetitions. Numbers in parentheses are CVs. T_1, T_2 and absolute concentrations are reported for all major singlets. B_{1+} was quantified using the reference water scan and used to constrain dictionary fitting for all other metabolites. The coupled metabolites in the phantom (mI, Glu, NAA multiplet, etc) were successfully fit (see Fig. 2h) but not quantified due to the lack of reliable T_1 and T_2 estimates for them.

Metabolite	**ΔConc (mM)**	**CRLB**	**ΔT_1 (ms)**	**ΔT_2 (ms)**	**B_{1+}**
NAA (2.01 ppm)	−0.1±0.5 (4.2%)	3.4%	−8±32 (4%)	−5±32 (6.4%)	N/A
Cr (3 ppm)	0.0±0.5 (4.8%)	3.4%	5±41 (6.7%)	5±32 (5.9%)	N/A
Cho (3.2 ppm)	−0.1±0.1 (3.4%)	5%	−13±43 (10.3%)	−1±32 (14.8%)	N/A
Water	N/A	N/A	−12±3 (0.5%)	−11±3 (1.1%)	1.13±0.01 (0.8%)

Table 2.

SNR comparisons between PRESS and MRSF, in both the phantom and in-vivo, based on numerical 3D Bloch spin simulations. Simulations were run for each singlet (NAA, Cr, Cho), using its mean measured T_1 and T_2 values, and averaged over all singlets. Note that, on average, T_1 values in the phantom are shorter than in-vivo, while T_2 values are longer. The SNR per unit time of the TR=1500 ms PRESS was normalized to one. The table demonstrates that using just the short echo time (TE=35 ms) scans of MRSF for metabolite quantification yields approximately 60% of the optimal PRESS SNR. However, since T_1 is often unknown in-vivo, acquisitions with prolonged TRs are preferred, such as a PRESS with TR=5000 ms; relative to such an acquisition, the TE=35 MRSF scans yield approximately 0.61/0.78≈80% of the SNR.

	Normalized Voxel Volume	**Weighted Voxel Volume**	**SNR per unit time**
Phantom (average over all singlets)			
PRESS (TR/TE=1500/35 ms)	0.87	0.48	1.00
PRESS (TR/TE=5000/35 ms)	0.87	0.54	0.59
MRSF (All TEs)	0.67	0.34	0.70
MRSF (TE=35 ms)	0.64	0.32	0.57
In-vivo (average over all singlets)			
PRESS (TR/TE=1500/35 ms)	0.87	0.48	1.00
PRESS (TR/TE=5000/35 ms)	0.87	0.68	0.78
MRSF (All TEs)	0.67	0.31	0.67
MRSF (TE=35 ms)	0.64	0.32	0.61

Table 3.

In-vivo quantification results. Mean±standard deviations are taken over all 14 subjects, and represent inter-subject statistics. The inter-scan, intra-subject coefficient of variation for each quantity – corresponding to the precision of our method – is shown in parentheses. Concentrations were calculated by fitting the summed TE=35 ms acquisitions using LCModel. CRLBs output by LCModel are averaged over all subjects. Shown are only those metabolites for which CRLB<20%. As with the phantom, T1 and T2 were only quantified for the singlets; B1+ was quantified using the reference water scan and used to constrain dictionary fitting for all other metabolites. To perform absolute quantification for coupled metabolites, average literature values for T1 and T2 were used, indicated by daggers (†). The transverse relaxation time of GSH was not found in the literature and a T2=100 ms was assumed (indicated by a double dagger). Table 3 shows that coupled metabolites can be successfully fit using the proposed method.

Metabolite	**Conc (mM)**	**CRLB**	**T_1 (ms)**	**T_2 (ms)**	**B_{1+}**
NAA (2.01 ppm)	12.5±1.1 (3.2%)	3.6%	1409±91 (4%)	168±13 (3%)	N/A
Cr (3 ppm)	7.4±0.7 (3.4%)	4.3%	1353±160 (5%)	126±12 (5%)	N/A
Cho (3.2 ppm)	2.4±0.3 (3.7%)	6.3%	1260±112 (5%)	174±20 (6%)	N/A
Glx	7.9±0.9 (5.4%)	8.7%	1200†	180†	N/A
GSH	1.8±0.5 (13%)	13.1%	397†	100††	N/A
mI	3.7±0.7 (6.4%)	8.6%	920†	196†	N/A
Water	N/A	N/A	1035±100 (2%)	70±4 (1%)	1.01±0.03 (0.4%)